Multifunctional semitransparent organic photovoltaics with high-throughput screened infrared reflector

Baozhong Deng, Kaiwen Zheng, Zihan Wang, Luqiao Yin, Hongliang Dong, Chengxi Zhang, Mona Tréguer-Delapierre, Kekeli N'KONOU, Bruno Grandidier, Shenghao Wang, et al.

To cite this version:

Baozhong Deng, Kaiwen Zheng, Zihan Wang, Luqiao Yin, Hongliang Dong, et al.. Multifunctional semitransparent organic photovoltaics with high-throughput screened infrared reflector. ACS Energy Letters, 2024, 9 (3), pp.976-984. 10.1021/acsenergylett.4c00149 . hal-04485009

HAL Id: hal-04485009
https://hal.science/hal-04485009v1

Submitted on 14 Mar 2024

Multifunctional Semitransparent Organic Photovoltaics with High-throughput Screened Infrared Reflector

Baozhong Deng,[†] *Kaiwen Zheng,*[†] *Zihan Wang,*[†] *Luqiao Yin,*[†] *Hongliang Dong,*[‡] *Chengxi Zhang,*[§] *Mona Treguer-Delapierre,*[¶] *Kekeli N'konou,*[⊥] *Bruno Grandidier,*[⊥] *Shenghao Wang,*[*,†] *Jianhua Zhang,*[*,†] *and Tao Xu*[*,†]

[†] School of Microelectronics and Materials Genome Institute, Shanghai University, 200444, Shanghai, China

[‡] Center for High Pressure Science and Technology Advanced Research, 201203, Shanghai, China

[§] School of Science, Jiangsu University of Science and Technology, 212100, Zhenjiang, China

[¶] Univ. Bordeaux, CNRS, Bordeaux INP, ICMCB, UMR 5026, F-33600 Pessac, France

[⊥] Univ. Lille, CNRS, Centrale Lille, Univ. Polytechnique Hauts-de-France, Junia-ISEN, UMR 8520 - IEMN, 59000, Lille, France

Corresponding Author

E-mail: shenghaowang@shu.edu.cn (S.W.), jhzhang@oa.shu.edu.cn (J.Z.), xtld@shu.edu.cn (T.X.)

ABSTRACT

Multifunctional semitransparent organic photovoltaics (ST-OPVs) combining power generation, light transparency and heat rejection have emerged as a promising technology for application in building-integrated photovoltaic systems, but maximizing all these features simultaneously is challenging. Herein, we show that high-throughput optical screening is essential to guide the design of infrared reflectors and enhance their synergy with the organic absorbers. Taking advantage of a volatile additive, 1,3,5-trichlorobenzene, to improve the crystallinity of the binary PM6:L8-BO active layer, we developed an optimized infrared reflector, consisting of a Na_3AlF_6 (160 nm)/ZnSe (190 nm) bilayer, which concomitantly increases all the key parameters of the reflector-free device. High-performance multifunctional ST-OPVs with a power conversion efficiency of 15.19%, an average photopic transmittance of 30.57%, a color rendering index of 81.86 and an infrared rejecting rate over 90% are demonstrated, providing practical prospects for future sustainable building-integrated photovoltaic systems.

TOC GRAPHICS

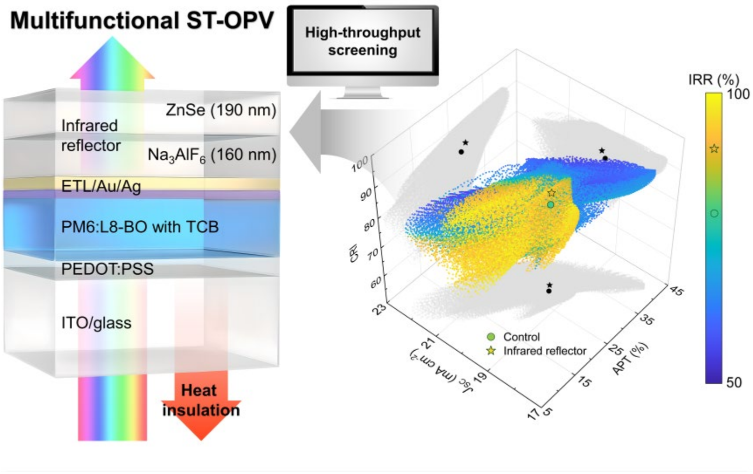

Among the wide range of photovoltaic applications, the development of building-integrated photovoltaic system (BIPV) has become essential to meet the demand for clean energy generation and saving in building, which is nowadays one of the fastest growing sectors in energy consumption.[1–5] In this respect, semitransparent organic photovoltaics (ST-OPVs) are attractive due to their unique feature that combines solar energy conversion and visible transparency.[6–12] Recent progress in nonfullerene acceptors (NFAs) with improved absorption in the near-infrared (NIR) wavelength range has led to performances of ST-OPVs surpassing their inorganic counterparts.[13–18] Further innovation in the absorbing materials has improved the two main competing indexes, the power conversion efficiency (PCE) and the average photopic transmittance (APT), leading to individually enhanced PCE of 12~14% and APT of 25~40%.[19–23] Besides, various optical engineering technologies have been applied to push the device performances. For example, the integration of a distributed Bragg reflector enhances NIR absorption.[24–30] Interestingly, it can also reject infrared radiations, providing a novel function to act as a heat insulator, which is evaluated by infrared rejecting rate (IRR).[31–35] Meanwhile, high color neutrality of the ST-OPVs with an excellent color rendering index (CRI) is also required to meet the aesthetic demand of BIPV.[36,37]

With the increase of indexes to make the ST-OPVs multifunctional, it is challenging to optimize the trade-off relationships existing among them. More specifically, the simultaneous improvement of all the key indexes in a single device has not been demonstrated. Indeed, an increase of the transparency usually implies a decrease of the PCE.[27,31-34] Conversely, delivering an improved PCE along with an IRR over 90%, which is the standard value for commercial solar film, reduces the APT to some extent.[38] As one function improves at the expense of the others or vice versa (see Table S1 for a review of the reported studies), high-throughput screening of the optical structures is becoming crucial to explore the parameter space for an acute selection of dielectric materials and the optimal design of the device configuration.[39,40] It provides a promising approach to engineer IR reflectors that maximize visible transparency and allow the bulk heterojunction (BHJ) to recycle NIR radiations, while rejecting the useless radiations that carry heat. This strategy goes beyond the refractive index matching of the optical structure, as it takes into account the optical properties of the entire device, so that an absolute maximum of multiple critical indexes can be targeted.

In this work, we start from exploiting a solid volatile additive approach to improve the crystallization process of the PM6:L8-BO BHJ active layer, enabling a PCE over 19% for the binary OPVs. Taking advantage of this high-performance OPV, we examine its coupling with an optical structure identified from high-throughput screening to assess the performances of multifunctional ST-OPVs. We show that a highly transparent dielectric infrared reflector (DIR) with a bilayer of Na_3AlF_6 (160 nm)/ZnSe (190 nm) allows to achieve a simultaneous enhancement of all the key indexes with respect to the DIR-free control device, yielding a PCE of 15.19%, an APT of 30.57%, a CRI of 81.86 and an IRR of 90.28%. The DIR does not only transmit the visible light efficiently and reflect the low energy infrared photons, but also enhances the exciton generation rate in the BHJ. Our multifunctional ST-OPVs combining power generation, transparency and heat rejection provide promising prospective for BIPV applications.

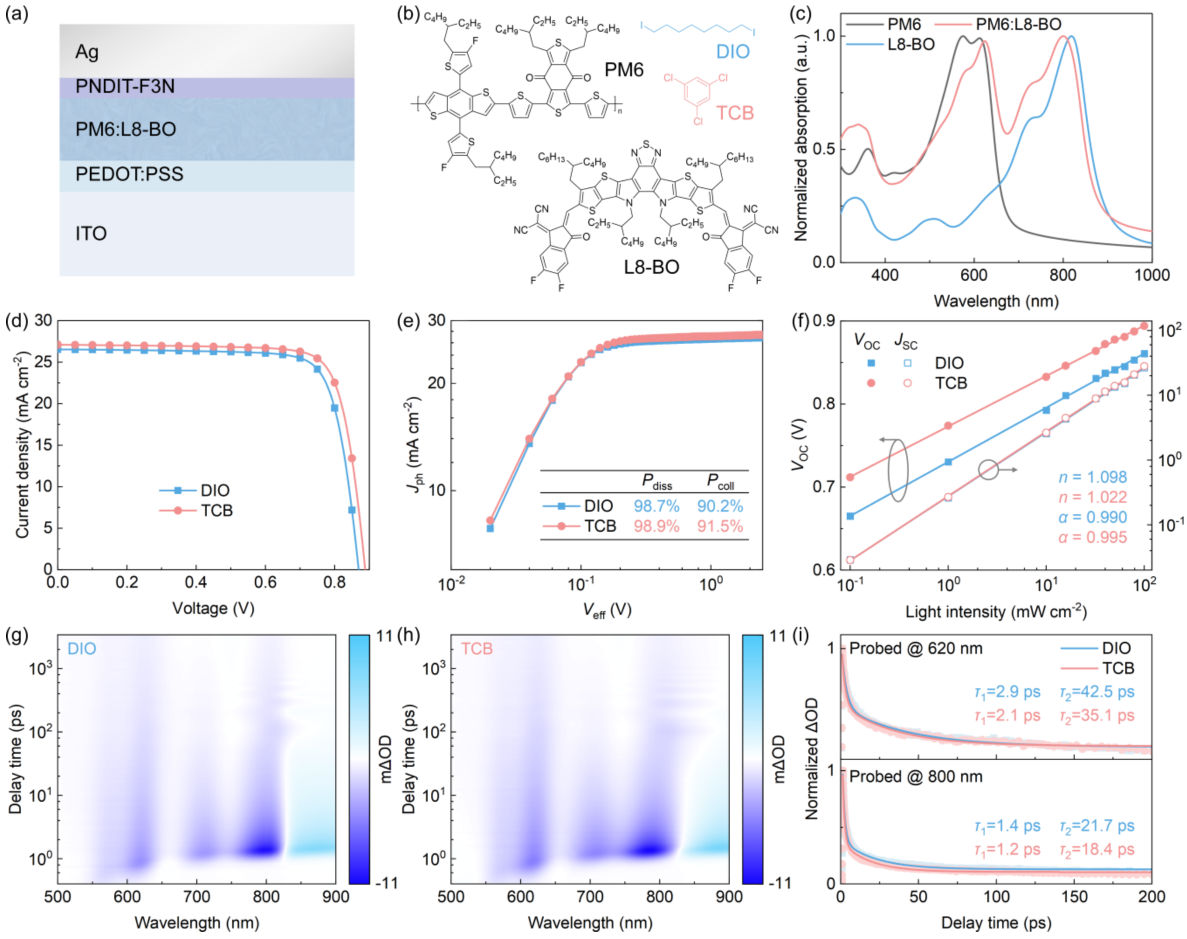

Figure 1. (a) Device structure of an opaque OPV. (b) Chemical structures of PM6, L8-BO, DIO and TCB. (c) Absorption spectra of PM6, L8-BO and PM6:L8-BO blend film. (d) J-V, (e) J_{ph}-V_{eff}, (f) V_{OC}-I and J_{SC}-I characteristics of the OPVs with DIO-treatment and with TCB-treatment. TA spectra of PM6:L8-BO BHJ (g) with DIO-treatment and (h) with TCB-treatment. (i) TA dynamics of the GSB signals probed at 620 nm and 800 nm for the BHJ films with DIO-treatment and with TCB-treatment.

A set of opaque OPVs was first fabricated, with the structure shown in Figure 1a: indium tin oxide (ITO)/poly(3,4-ethylenedioxythiophene):poly(styreneesulfonate)(PEDOT:PSS)/BHJ/Poly[[2,7-bis(2-ethylhexyl)-1,2,3,6,7,8-hexahydro-1,3,6,8-tetraoxobenzo[lmn][3,8]phenanthroline-4,9-diyl]-2,5-thiophenediyl[9,9-bis[3'((N,N-dimethyl)-N-ethylamino)propyl]-9Hfluorene-2,7-diyl]-2,5-thiophenediyl] (PDNIT-F3N)/Ag. The 30 nm-thick PEDOT:PSS and 10 nm-thick PNDIT-F3N were used as the hole transport layer (HTL) and electron transport layer (ETL), respectively. Nb_2C MXene was iintegrated in PEDOT:PSS to improve the conductivity of HTL, as reported in our previous work.[41] The BHJ active layer consisted of a binary blend film of PM6:L8-BO with the chemical structures drawn in Figure 1b and their respective absorption spectra as well as the spectrum of the blend film shown Figure 1c. PM6 exhibits an absorption ranging from 450 to 700 nm, while L8-BO has complementary absorption in the NIR region. The use of solvent additive in the active layer was studied by using the benchmark liquid additive 1,8-diiodooctane (DIO) and the solid volatile additive 1,3,5-trichlorobenzene (TCB). Their concentration was delicately optimized (Figure S1 and S2, Table S2 and S3). The current density-voltage (*J*-*V*) characteristics of optimal OPVs with DIO or TCB treatments are shown in Figure 1d. A PCE of 19.10%, with a short circuit current J_{SC} of 27.09 mA cm^{-2}, an open circuit voltage V_{OC} of 0.89 V and a fill factor FF of 79.4%, were obtained for the TCB-based device, higher than that of the DIO-treated device (18.19%) (see Table 1).

Table 1. Summary of photovoltaic parameters measured for the DIO-treated OPVs and the TCB-treated OPVs. The results were averaged from the measurements of 12 cells.

Treatment	V_{OC} (V)	J_{SC} (mA cm^{-2})	J_{cal} (mA cm^{-2})	FF (%)	PCE (%)
DIO	0.87±0.01	26.53±0.36	25.92	78.9±0.4	18.19±0.23
TCB	0.89±0.01	27.09±0.35	26.35	79.4±0.2	19.10±0.22

To gain physical insight into the superiority of TCB, the exciton dissociation, charge recombination and collection properties were systematically studied. Based on the photocurrent density (J_{ph})-effective voltage (V_{eff}) characteristics of the OPVs (Figure 1e), the exciton dissociation probabilities (P_{diss}) and charge collection probabilities (P_{coll}) were calculated (Note S1). The TCB-based device exhibits a P_{diss} of 98.9% and a P_{coll} of 91.5% higher than those of the DIO-based device (P_{diss} of 98.7% and P_{coll} of 90.2%), indicating that the use of TCB improves the charge collection capacity of the active layer. In addition, the charge recombination process was evaluated by plotting J_{SC} and V_{OC} versus the light intensity (Figure 1f). Their dependence, outlined by the factors α and n (Note S2), yields an α of 0.995 for the TCB-based device, higher than that of the DIO-based device (0.990). Meanwhile, the TCB-based device shows a lower n value (1.022) than that of the DIO-based device (1.098). Both results suggest that the TCB-treatment effectively suppresses the bimolecular and monomolecular recombination.[42] The photoinduced charge transfer dynamics were further investigated with transient absorption (TA) measurements. As shown in Figure 1g and 1h, the TCB-treatment gives a higher ground state bleaching (GSB) signal intensity compared to the DIO-treatment, indicating an enhanced carrier transport. The fits of the PM6 GSB and L8-BO GSB signals reveal that the charge transport involves a fast process lifetime τ_1 that is related to the exciton dissociation time, and a slow process lifetime τ_2 assigned to the exciton diffusion and recombination time (Figures 1i and S3). For hole transport, both lifetimes τ_1 (2.1 ps) and τ_2 (35.1 ps) are shorter in the TCB-based film compared to the DIO-based film (2.9 ps and 42.5 ps). Similar shorter lifetimes are obtained in the TCB-based film for electrons, giving evidence of a more rapid exciton dissociation at the donor-acceptor interfaces and a faster diffusion of excitons toward the interfaces before dissociation.[43] These results demonstrate that the TCB-treatment accelerates the charge transfer kinetics and enhances the charge collection through mitigation of the charge recombination.

The surface and crystalline properties of the BHJ films with different additives were further analyzed to assess the impact of the film morphology on the electrical properties. First, the root-mean-roughness (RMS) measured in the atomic force microscopy (AFM) images of the DIO and TCB-based BHJ films (Figure 2a and 2b, respectively) is significantly reduced for the film with TCB-treatment (0.71 nm) in comparison with the DIO-based film (1.54 nm). This observation accounts for the TCB-induced red-shift in the absorption peak of L8-BO (Figure S4), which indicates that the addition of TCB affects the molecular aggregation of the acceptor, leading to enhanced crystallinity of the active layer.[44] It is also supported by the transmission electron microscopy (TEM) measurements, which show a stronger inhomogeneous contrast in the DIO-based film pointing again to an excessive aggregation of the L8-BO molecules (Figure 2c and 2d). The molecular orientation and crystalline properties were subsequently studied with grazing incidence wide-angle X-ray scattering (GIWAXS), as shown in Figure 2e and 2f. Both films show a face-on orientation with evident scattering in the out-of-plane direction (1.71 $Å^{-1}$) and in-plane direction (0.33 $Å^{-1}$), which represent the (010) π-π stacking and (100) lamellar stacking, respectively (Figure 2g). It reveals that the TCB-treated film shows a lower π-π stacking d-spacing of 3.707 Å and a longer crystalline coherence length (CCL) of 42.24 Å (Table S4 and Note S3) compared to the DIO-treated film (3.723 Å and 37.89 Å), indicating reinforced molecular packing and improved crystallinity for the BHJ active layer.

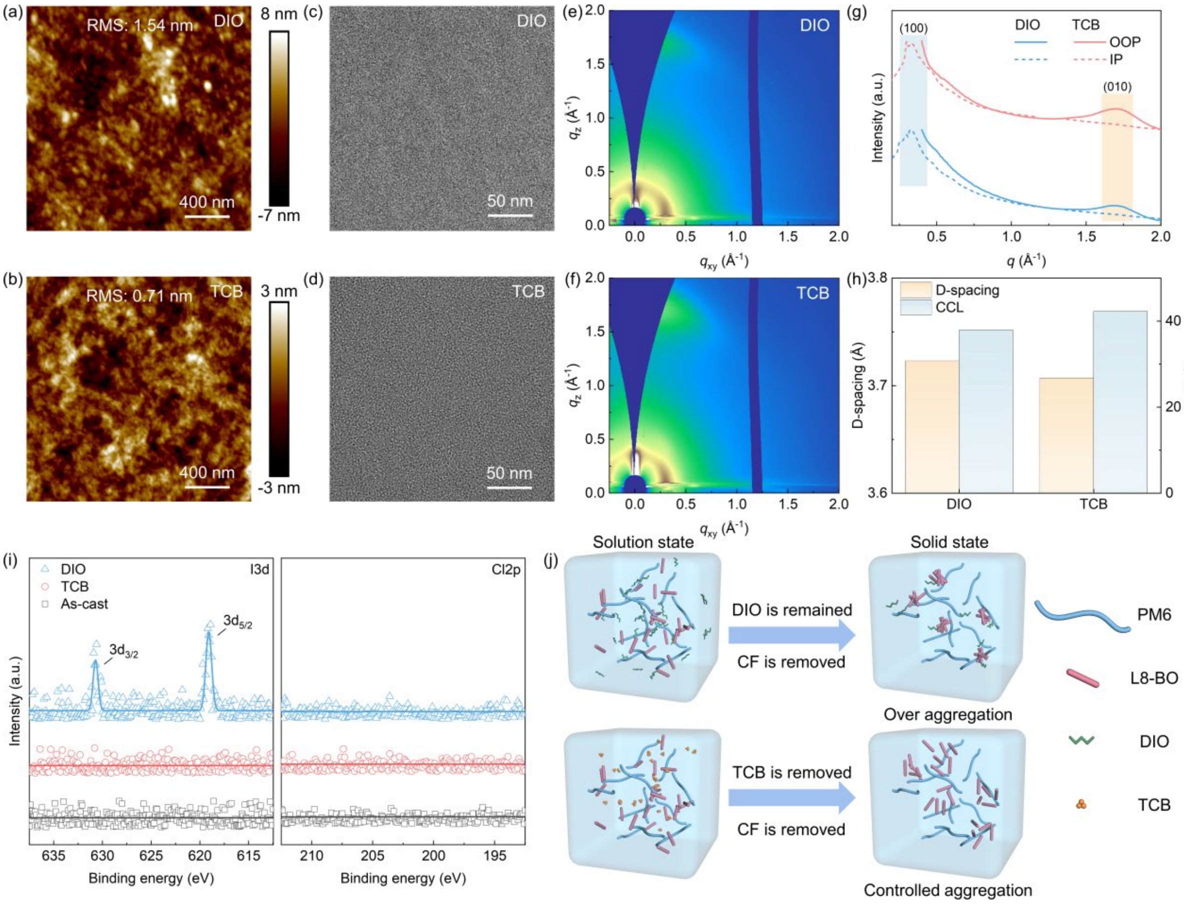

Figure 2. AFM images measured for the PM6:L8-BO blend films (a) with DIO-treatment and (b) with TCB-treatment. TEM images measured for the PM6:L8-BO blend films (c) with DIO-treatment and (d) with TCB-treatment. (g) GIWAXS 1D profiles along the IP and OOP directions and (h) CCL results measured for the PM6:L8-BO blend films with DIO-treatment and TCB-treatment. (i) XPS (I3d and Cl2p) spectra measured for the PM:L8-BO blend films with DIO-treatment and TCB-treatment. (j) Schematic diagram of the working mechanism induced by the additives.

X-ray photoelectron spectroscopy (XPS) measurements were performed to determine the interplay between the crystallinity and the presence of the additives in the BHJ. As shown in Figure 2i, the DIO-treated film shows an extra I3d binding signal compared with the as-cast film. Thus, DIO does not fully volatize, causing the over aggregation of L8-BO molecules during the film formation of the BHJ.[45-47] Fourier transform infrared (FTIR) measurements also confirmed such an observation (Figure S5). Conversely, the absence of Cl signal related to TCB supports an improved volatility, which reduces the aggregation of L8-BO molecules to enable the formation of a favorable BHJ morphology (see Figure 2j), thereby accounting for the improved PCE.[48]

Taking advantage of the low recombination loss and superior morphological properties, the TCB-treated PM6:L8-BO binary active layer was selected for the ST-OPV fabrication, as it does not affect the visible transparency of the active layer (Figure S6). A set of ST-OPVs was subsequently fabricated by using a bilayer semitransparent electrode of Au (1 nm)/Ag (10 nm) instead of the opaque metallic electrode. The ultrathin Au interlayer improves the wettability and favors the formation of a uniform upper Ag contact,[49] as shown in the scanning electron microscope (SEM) observations (Figure S7). The APT of the ST-OPVs is calculated using the following equation:

$$\mathrm{APT} = \frac{\int_{380}^{780} \mathrm{T}(\lambda)\mathrm{V}(\lambda)\mathrm{F}(\lambda)\mathrm{d}\lambda}{\int_{380}^{780} \mathrm{V}(\lambda)\mathrm{F}(\lambda)\mathrm{d}\lambda} \tag{1}$$

where T(λ) is the transmission spectrum of the ST-OPVs, V(λ) is the human eye response spectrum and F(λ) is the power irradiation of AM1.5G. The PM6:L8-BO ratio and BHJ thickness were optimized in order to improve the light utilization efficiency (LUE) that corresponds to the product of PCE and APT values (Figure S8 and S9, Table S5 and S6). A ST-OPV with a 95 nm-thick BHJ and a weight ratio of 0.6:1.2 for PM6:L8-BO, yielding a PCE of 13.47%, an APT of 27.23% and a LUE of 3.68%, was considered as the control device.

To further improve the performance of ST-OPVs, a highly transparent DIR was applied upon the Au/Ag electrode to enhance simultaneously the power generation, see-through and heat insulation functions. In particular, the heat insulation is evaluated by the figure-of-merit IRR defined as follows:

$$\mathrm{IRR} = \frac{\int_{780}^{2500} \mathrm{T}(\lambda)\mathrm{F}(\lambda)\mathrm{d}\lambda}{\int_{780}^{2500} \mathrm{F}(\lambda)\mathrm{d}\lambda} \tag{2}$$

As illustrated in Figure S10 and described in the Supporting Information, an optical model based on the transfer matrix method (TMM) was developed to simulate the optical behaviors of the device including reflection, transmission and absorption as a function of the optical constants and geometrical parameters of each functional layer. It gives access to the key parameters of ST-OPVs, such as J_{SC}, APT, CRI and IRR (Figure S11). Based on the measured wavelength-dependent refractive indices and extinction coefficients of the different layers used in the control device (Figure S12), high-throughput optical screening was performed to predict the optimal configuration of the DIR, in which the refractive indices n_1 and n_2 of potential dielectric materials were varied from 1.0 to 3.0 with an interval of 0.1 and their layer thicknesses d_1 and d_2 were varied from 0 to 200 nm with an interval of 10 nm. A total of 194, 481 device configurations were simulated to find out the maximal enhancement of the multiple key parameters.

Figure 3 presents a three-dimensional contour map of the simulated J_{SC}, APT, CRI and IRR as a function of the DIR configuration. The high-throughput optical screening reveals that all relevant parameters can be simultaneously improved from an appropriate choice of the dielectric indices and thicknesses, reaching an optimal bilayer DIR configuration of (n_1=1.3, d_1=160 nm)/(n_2=2.6, d_2=190 nm), as detailed in the projected views of Figure S13. Among the realistic dielectric materials that can be thermally evaporated, Na_3AlF_6 and ZnSe have refractive indices close to the predicted values. The optimal device (star symbol) with a DIR consisting of Na_3AlF_6 (160 nm)/ZnSe (190 nm) shows not only an improvement of J_{SC}, APT and CRI, but also a significant enhancement of IRR compared to the DIR-free simulated device (circle symbol). To account for this positive impact, the optical field $\left|\frac{|\boldsymbol{E}|}{|\boldsymbol{E}_0|}\right|^2$ in the whole structure was also simulated (Figure 3b and 3c). The optimal device exhibits enhanced transmission in the visible wavelength range (400-600 nm) and stronger reflection intensity in the NIR wavelength (780-2500 nm). From the calculation of the exciton generation rate (Figure S14), a stronger exciton generation occurs in the range of 780-900 nm due to the re-harvesting of the NIR photons in the BHJ.

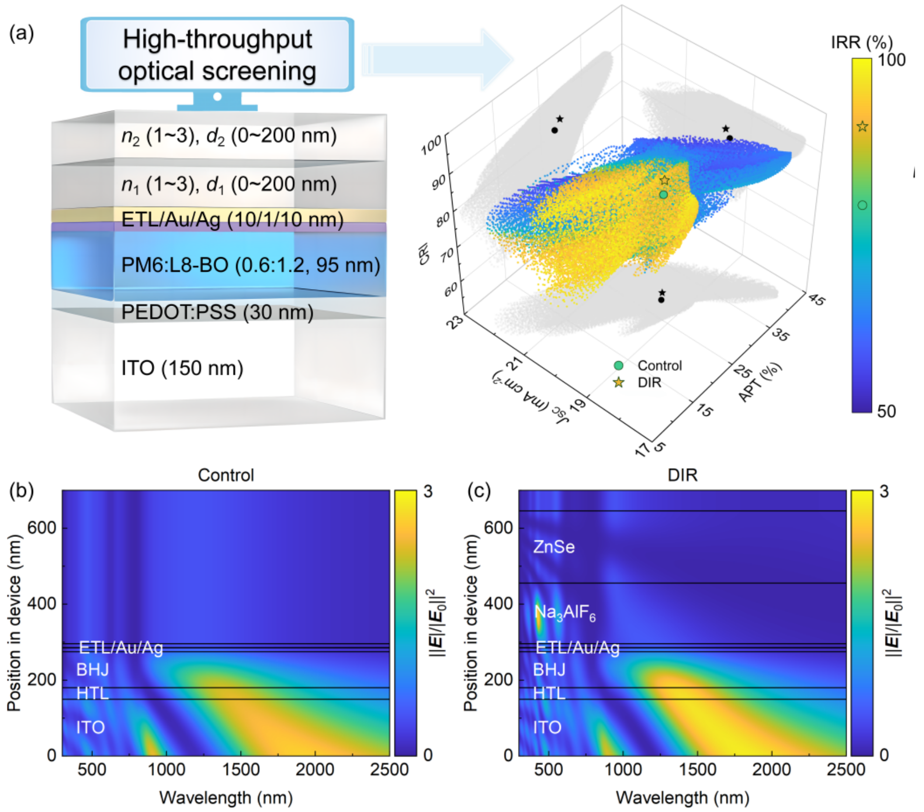

Figure 3. (a) Device structure of the ST-OPVs with DIR (left) and the simulated J_{SC}-APT-CRI-IRR contour map as a function of the refractive index and layer thickness of the DIR

(right). Profiles of the electrical field distribution calculated for (b) the control ST-OPV without DIR and (c) the ST-OPV with DIR.

On the basis of the aforementioned simulations, ST-OPVs with and without the DIR were fabricated. In addition, core-bishell PdCu@Au@SiO_2 nanotripods with NIR-customized localized surface plasmon resonance (LSPR), synthesized by combining a seed-mediated growth method for tripod synthesis with a Stöber method for silica encapsulation (Figure S15), were introduced in the active layer to achieve NIR absorption enhancement and scattering optimization, leading to enhanced device PCE (Figure S16 and Table S7). A nanostructured anti-reflection coating was also applied on the front side of the glass substrates to reduce the reflection loss, as optimized in our previous work.[50]

The *J-V* characteristics, EQE and transmission spectra measured for the control device and the optimal ST-OPVs are shown in Figure 4a and 4b, respectively. The corresponding photovoltaic parameters are listed in Table 2 and clearly show that PCE, APT, LUE, CRI and IRR of the optimal device are all improved with the DIR, consistent with the simulated prediction. Photographs of the control device and the optimal ST-OPV (Figure 4b) exhibit improved visible transparency and color neutrality for the optimal ST-OPVs, which are further confirmed by the observation of the Commission Internationale de l'Éclairage (CIE) coordinates in Figure 4c. The advantage of our optical engineering strategy is clearly demonstrated in the spider diagram of Figure 4d, revealing that all the indexes have been concomitantly enhanced. To date, a PCE of 15.19%, an APT of 33.02%, a LUE of 4.64%, a CRI of 81.86% and an IRR of 90.28%, represent among the best-performing reported multifunctional ST-OPVs to our knowledge, as shown in Figure 4e and Table S1. Another figure of merit, the quantum utilization efficiency, $\mathrm{QUE}(\lambda) = \mathrm{EQE}(\lambda) + T(\lambda)$, yields values below the transmittance of ITO/glass (Figure S17), confirming the reliability of our results.

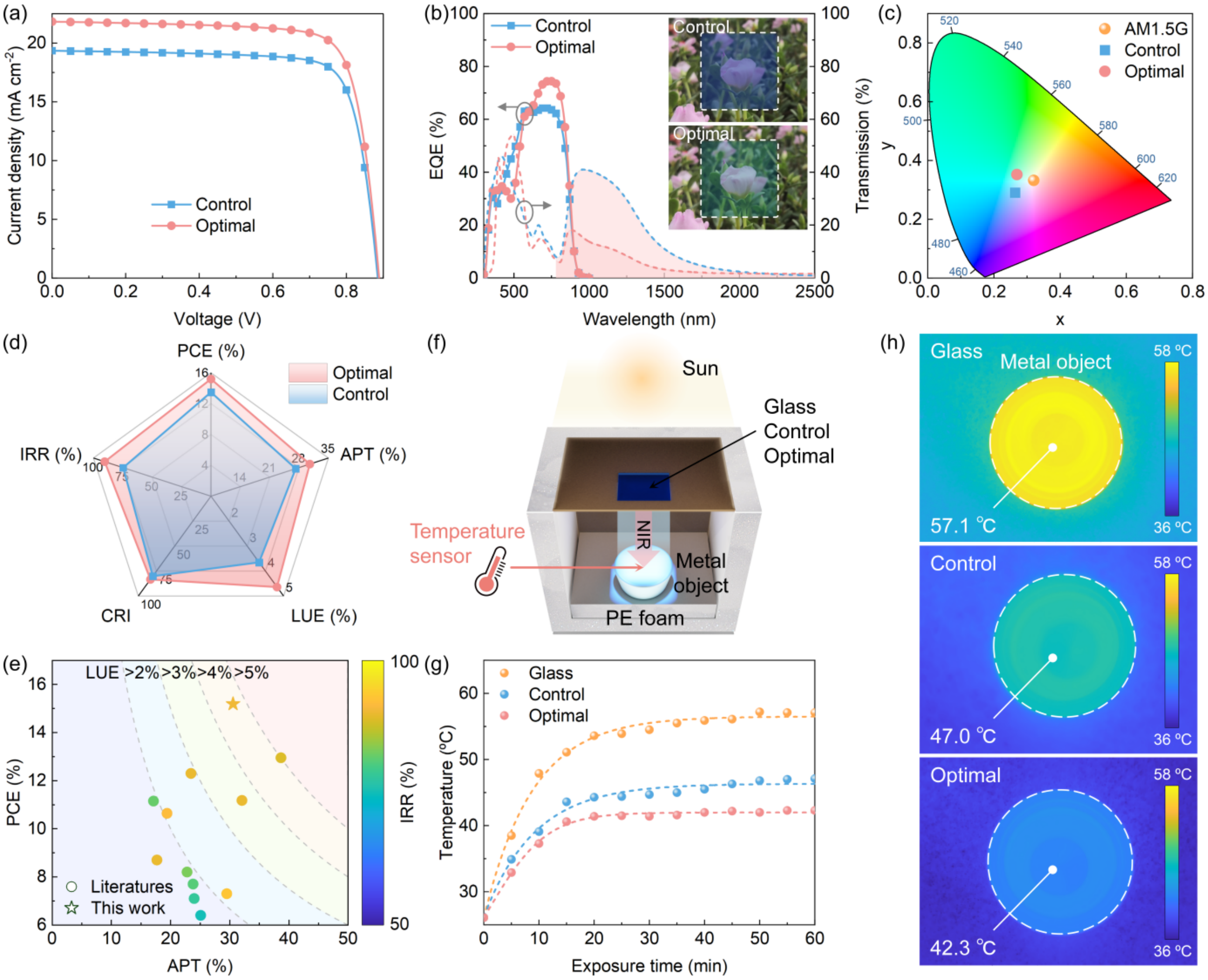

Figure 4. (a) *J*-*V* characteristics, (b) EQE and transmission spectra, and (c) chromaticity coordinates measured for the control device and the optimal ST-OPVs with a DIR of Na_3AlF_6(160 nm)/ZnSe(190 nm). (d) Comparison of device performance, including PCE, APT, LUE, CRI and IRR for the control device and the optimal ST-OPV. (e) Comparison of the PCE, APT, LUE, CRI and IRR values between the optimal ST-OPVs demonstrated in this work and those reported in the literature listed in Table S1. (f) Schematic diagram of the room simulator, and (g) the temperature measured for the metal object with different radiation medium (glass,

the control ST-OPV and the optimal ST-OPV). (h) IR heat images of the metal object sheltered by glass, the control ST-OPV and the optimal ST-OPV after 60 minutes of illumination.

Finally, to demonstrate the heat-insulation function, a room simulator consisting of a polyethylene foam box, a metal object with high thermal conductivity and a temperature sensor was built (Figure 4f). The simulator was placed outdoor under real summer condition (August, Shanghai). The heat insulation is clearly observed by tracing the temperature of the metal object with different radiation medium (glass, the control ST-OPV and the optimal ST-OPV), as shown in Figure 4g. After a 60 min-long exposure, the optimal ST-OPV-sheltered object shows the lowest temperature of 42.3°C, compared to that of the control ST-OPV-sheltered one (47°C) and the glass-sheltered one (57.1°C), demonstrating a heat insulating property prized for energy savings in BIPV.[51]

Table 2. Summary of multifunctional parameters measured for the 95 nm-thick PM6:L8-BO (0.6:1.2)-based control device, and the optimal ST-OPVs with DIR of Na_3AlF_6(160 nm)/ZnSe(190 nm). The results were averaged from the measurements of 12 cells.

Device	V_{OC} (V)	J_{SC} (mA.cm^{-2})	J_{cal} (mA cm^{-2})	FF (%)	PCE (%)	APT (%)	LUE (%)	CRI	IRR (%)
Control	0.89±0.01	19.35±0.29	18.52	78.8±0.3	13.50±0.20	27.23±0.32	3.68±0.06	80.75±0.92	75.70±1.36
Optimal	0.89±0.01	21.82±0.40	21.04	78.3±0.5	15.19±0.22	30.57±0.43	4.64±0.07	81.86±1.44	90.28±0.44

In summary, we have developed multifunctional ST-OPVs with excellent energy generation and heat-insulation features together with a good see-through function by using a strategy combining material innovation and optical engineering. The use of TCB as a volatile additive improves the BHJ structural quality, leading to efficient OPVs with reduced non-radiative recombination loss. The further integration of a highly transparent DIR identified from high-throughput optical screening is key to shape the transmitted light, harvest additional NIR photons and reflect the useless radiations that carry heat. As a consequence, all the competing indexes have been simultaneously raised within one device, which can greatly accelerate future applications of ST-OPVs in BIPV.

ASSOCIATED CONTENT

Supporting Information. Experimental details; supplementary notes for P_{diss} and P_{coll} calculation, light dependence analysis and Crystallinity analysis; supplementary *J*-*V* and EQE curves; absorption and transmission spectra; refractive indexes and extinction coefficients; electrical field profiles; dark *J*-*V* curves; summary of multifunctional ST-OPVs reported recent years.

AUTHOR INFORMATION

Corresponding Author

*E-mail: shenghaowang@shu.edu.cn (S.W.).

*E-mail: jhzhang@oa.shu.edu.cn (J.Z.)

*E-mail: xtld@shu.edu.cn (T.X.).

Author Contributions

T.X. and S.W. conceived and directed this project. B.D. conducted the device fabrication and data analysis. B.D. and K.Z. conducted the electrical characterization. Z.W. performed the morphological observations. L.Y. and J.Z conducted IR heat analysis. H.D. performed GIWAXS measurements. C.Z. performed the transient absorption spectroscopy. M.T. performed the synthesis of nanotripods. T.X. J.Z and S.W. wrote the manuscript. B.G. and K.N. contributed to revisions of the manuscript.

Notes

The authors declare no competing financial interest.

ACKNOWLEDGMENT

This work was financially supported by the open research fund of Songshan Lake Materials Laboratory (No. 2021SLABFK09) and the National Natural Science Foundations of China (12174244 and 52102182). S. W. acknowledges funding support from the Program for Professor of Special Appointment (Eastern Scholar) at the Shanghai Institutions of Higher Learning and the Shanghai Rising-Star Program (19QA1403800). The authors gratefully acknowledge BSRF-1W1A beamline for the help in characterizations.

REFERENCES

(1) Jiang, K.; Zhang, J.; Zhong, C.; Lin, F. R.; Qi, F.; Li, Q.; Peng, Z.; Kaminsky, W.; Jang, S.-H.; Yu, J.; Deng, X.; Hu, H.; Shen, D.; Gao, F.; Ade, H.; Xiao, M.; Zhang, C.; Jen, A. K.-Y.

Suppressed Recombination Loss in Organic Photovoltaics Adopting a Planar–Mixed Heterojunction Architecture. *Nat. Energy* **2022**, *7* (11), 1076–1086.

(2) Yoon, S.; Park, S.; Park, S. H.; Nah, S.; Lee, S.; Lee, J.-W.; Ahn, H.; Yu, H.; Shin, E.-Y.; Kim, B. J.; Min, B. K.; Noh, J. H.; Son, H. J. High-Performance Scalable Organic Photovoltaics with High Thickness Tolerance from 1 cm^2 to above 50 cm^2. *Joule* **2022**, *6* (10), 2406–2422.

(3) Kim, D. H.; Wibowo, F. T. A.; Lee, D.; Krishna, N. V.; Park, S.; Cho, S.; Jang, S. Non-Fullerene-Based Inverted Organic Photovoltaic Device with Long-Term Stability. *Energy Environ. Mater.* **2023**, *6* (3), e12381.

(4) Yang, X.; Li, B.; Zhang, X.; Li, S.; Zhang, Q.; Yuan, L.; Ko, D.; Ma, W.; Yuan, J. Intrinsic Role of Volatile Solid Additive in High-Efficiency PM6:Y6 Series Nonfullerene Solar Cells. *Adv. Mater.* **2023**, 2301604.

(5) Song, X.; Xu, H.; Jiang, X.; Gao, S.; Zhou, X.; Xu, S.; Li, J.; Yu, J.; Liu, W.; Zhu, W.; Müller-Buschbaum, P. Film-Formation Dynamics Coordinated by Intermediate State Engineering Enables Efficient Thickness-Insensitive Organic Solar Cells. *Energy Environ. Sci.* **2023**, *16* (8), 3441–3452.

(6) Li, Y.; Guo, X.; Peng, Z.; Qu, B.; Yan, H.; Ade, H.; Zhang, M.; Forrest, S. R. Color-Neutral, Semitransparent Organic Photovoltaics for Power Window Applications. *Proc. Natl. Acad. Sci. U.S.A.* **2020**, *117* (35), 21147–21154.

(7) Wang, S.; Zhao, Y.; Lian, H.; Peng, C.; Yang, X.; Gao, Y.; Peng, Y.; Lan, W.; Elmi, O. I.; Stiévenard, D.; Wei, B.; Zhu, F.; Xu, T. Towards All-Solution-Processed Top-Illuminated Flexible Organic Solar Cells Using Ultrathin Ag-Modified Graphite-Coated Poly(Ethylene Terephthalate) Substrates. *Nanophotonics* **2019**, *8* (2), 297–306.

(8) Burgués-Ceballos, I.; Lucera, L.; Tiwana, P.; Ocytko, K.; Tan, L. W.; Kowalski, S.; Snow, J.; Pron, A.; Bürckstümmer, H.; Blouin, N.; Morse, G. Transparent Organic Photovoltaics: A Strategic Niche to Advance Commercialization. *Joule* **2021**, *5* (9), 2261–2272.

(9) Lie, S.; Bruno, A.; Wong, L. H.; Etgar, L. Semitransparent Perovskite Solar Cells with > 13% Efficiency and 27% Transperancy Using Plasmonic Au Nanorods. *ACS Appl. Mater. Interfaces* **2022**, *14* (9), 11339–11349.

(10) Cheng, H.; Zhao, Y.; Yang, Y. Toward High-Performance Semitransparent Organic Photovoltaics with Narrow-Bandgap Donors and Non-Fullerene Acceptors. *Adv. Energy Mater.* **2022**, *12* (3), 2102908.

(11) Jing, J.; Dong, S.; Zhang, K.; Zhou, Z.; Xue, Q.; Song, Y.; Du, Z.; Ren, M.; Huang, F. Semitransparent Organic Solar Cells with Efficiency Surpassing 15%. *Adv. Energy Mater.* **2022**, *12* (20), 2200453.

(12) Xie, D.; Zhang, Y.; Yuan, X.; Li, Y.; Huang, F.; Cao, Y.; Duan, C. A 2.20 eV Bandgap Polymer Donor for Efficient Colorful Semitransparent Organic Solar Cells. *Adv. Funct. Mater.* **2023**, *33* (11), 2212601.

(13) Yuan, J.; Zhang, Y.; Zhou, L.; Zhang, G.; Yip, H.-L.; Lau, T.-K.; Lu, X.; Zhu, C.; Peng, H.; Johnson, P. A.; Leclerc, M.; Cao, Y.; Ulanski, J.; Li, Y.; Zou, Y. Single-Junction Organic Solar Cell with over 15% Efficiency Using Fused-Ring Acceptor with Electron-Deficient Core. *Joule* **2019**, *3* (4), 1140–1151.

(14) Xu, T.; Gong, C.; Wang, S.; Lian, H.; Lan, W.; Lévêque, G.; Grandidier, B.; Plain, J.; Bachelot, R.; Wei, B.; Zhu, F. Ultraviolet-Durable Flexible Nonfullerene Organic Solar Cells Realized by a Hybrid Nanostructured Transparent Electrode. *Sol. RRL* **2020**, *4* (5), 1900522.

(15) Cui, Y.; Xu, Y.; Yao, H.; Bi, P.; Hong, L.; Zhang, J.; Zu, Y.; Zhang, T.; Qin, J.; Ren, J.; Chen, Z.; He, C.; Hao, X.; Wei, Z.; Hou, J. Single-Junction Organic Photovoltaic Cell with 19% Efficiency. *Adv. Mater.* **2021**, *33* (41), 2102420.

(16) Sun, R.; Wu, Y.; Yang, X.; Gao, Y.; Chen, Z.; Li, K.; Qiao, J.; Wang, T.; Guo, J.; Liu, C.; Hao, X.; Zhu, H.; Min, J. Single-Junction Organic Solar Cells with 19.17% Efficiency Enabled by Introducing One Asymmetric Guest Acceptor. *Adv. Mater.* **2022**, *34* (26), 2110147.

(17) Li, Y.; Huang, X.; Sheriff, H. K. M.; Forrest, S. R. Semitransparent Organic Photovoltaics for Building-Integrated Photovoltaic Applications. *Nat. Rev. Mater.* **2022**, *8* (3), 186–201.

(18) Zheng, X.; Zuo, L.; Yan, K.; Shan, S.; Chen, T.; Ding, G.; Xu, B.; Yang, X.; Hou, J.; Shi, M.; Chen, H. Versatile Organic Photovoltaics with a Power Density of Nearly 40 W g $^{-1}$. *Energy Environ. Sci.* **2023**, *16* (5), 2284–2294.

(19) Chang, Y.; Zhu, X.; Zhu, L.; Wang, Y.; Yang, C.; Gu, X.; Zhang, Y.; Zhang, J.; Lu, K.; Sun, X.; Wei, Z. Regioregular Narrow Bandgap Copolymer with Strong Aggregation Ability for High-Performance Semitransparent Photovoltaics. *Nano Energy* **2021**, *86*, 106098.

(20) Huang, X.; Zhang, L.; Cheng, Y.; Oh, J.; Li, C.; Huang, B.; Zhao, L.; Deng, J.; Zhang, Y.; Liu, Z.; Wu, F.; Hu, X.; Yang, C.; Chen, L.; Chen, Y. Novel Narrow Bandgap Terpolymer Donors Enables Record Performance for Semitransparent Organic Solar Cells Based on All-Narrow Bandgap Semiconductors. *Adv. Funct. Mater.* **2022**, *32* (5), 2108634.

(21) Huang, X.; Cheng, Y.; Fang, Y.; Zhang, L.; Hu, X.; Jeong, S. Y.; Zhang, H.; Woo, H. Y.; Wu, F.; Chen, L. A Molecular Weight-Regulated Sequential Deposition Strategy Enabling

Semitransparent Organic Solar Cells with the Light Utilization Efficiency of over 5%. *Energy Environ. Sci.* **2022**, *15* (11), 4776–4788.

(22) Zhang, Y.; Zheng, J.; Jiang, Z.; He, X.; Kim, J.; Xu, L.; Qin, M.; Lu, X.; Kyaw, A. K. K.; Choy, W. C. H. Guided-Growth Ultrathin Metal Film Enabled Efficient Semi-Transparent Organic Solar Cells. *Adv. Energy Mater.* **2023**, *13* (7), 2203266.

(23) Zhao, L.; Huang, X.; Wang, Y.; Young Jeong, S.; Huang, B.; Deng, J.; Liu, J.; Cheng, Y.; Young Woo, H.; Wu, F.; Chen, L.; Chen, L. Combination of Highly Photovoltaic and Highly Transparent Materials Enables Record Performance Semitransparent Organic Solar Cells. *Chem. Eng. J.* **2023**, *451*, 139081.

(24) Dudem, B.; Jung, J. W.; Yu, J. S. Improved Light Harvesting Efficiency of Semitransparent Organic Solar Cells Enabled by Broadband/Omnidirectional Subwavelength Antireflective Architectures. *J. Mater. Chem. A* **2018**, *6* (30), 14769–14779.

(25) Li, Y.; Ji, C.; Qu, Y.; Huang, X.; Hou, S.; Li, C.; Liao, L.; Guo, L. J.; Forrest, S. R. Enhanced Light Utilization in Semitransparent Organic Photovoltaics Using an Optical Outcoupling Architecture. *Adv. Mater.* **2019**, *31* (40), 1903173.

(26) Jiang, B.-H.; Lee, H.-E.; Lu, J.-H.; Tsai, T.-H.; Shieh, T.-S.; Jeng, R.-J.; Chen, C.-P. High-Performance Semitransparent Organic Photovoltaics Featuring a Surface Phase-Matched Transmission-Enhancing Ag/ITO Electrode. *ACS Appl. Mater. Interfaces* **2020**, *12* (35), 39496–39504.

(27) Guan, S.; Li, Y.; Yan, K.; Fu, W.; Zuo, L.; Chen, H. Balancing the Selective Absorption and Photon-to-Electron Conversion for Semitransparent Organic Photovoltaics with 5.0% Light-Utilization Efficiency. *Adv. Mater.* **2022**, *34* (41), 2205844.

(28) Liu, X.; Zhong, Z.; Zhu, R.; Yu, J.; Li, G. Aperiodic Band-Pass Electrode Enables Record-Performance Transparent Organic Photovoltaics. *Joule* **2022**, *6* (8), 1918–1930.

(29) Deng, B.; Shen, Y.; Zheng, K.; Wang, C.; Lévêque, G.; Xu, T. Dual Photonic Structures Enable High-Performance Semitransparent Organic Photovoltaics with Enhanced Light Utilization. *Sol. RRL* **2023**, *7* (13), 2300211.

(30) Zhao, Y.; Zheng, K.; Ning, J.; Xu, T.; Wang, S. Plasmonics in Organic Solar Cells: Toward Versatile Applications. *ACS Appl. Electron. Mater.* **2023**, *5* (2), 632–641.

(31) Sun, C.; Xia, R.; Shi, H.; Yao, H.; Liu, X.; Hou, J.; Huang, F.; Yip, H.-L.; Cao, Y. Heat-Insulating Multifunctional Semitransparent Polymer Solar Cells. *Joule* **2018**, *2* (9), 1816–1826.

(32) Wang, D.; Qin, R.; Zhou, G.; Li, X.; Xia, R.; Li, Y.; Zhan, L.; Zhu, H.; Lu, X.; Yip, H.; Chen, H.; Li, C. High-Performance Semitransparent Organic Solar Cells with Excellent Infrared Reflection and See-Through Functions. *Adv. Mater.* **2020**, *32* (32), 2001621.

(33) Li, X.; Xia, R.; Yan, K.; Yip, H.-L.; Chen, H.; Li, C.-Z. Multifunctional Semitransparent Organic Solar Cells with Excellent Infrared Photon Rejection. *Chin. Chem. Lett.* **2020**, *31* (6), 1608–1611.

(34) Wang, D.; Li, Y.; Zhou, G.; Gu, E.; Xia, R.; Yan, B.; Yao, J.; Zhu, H.; Lu, X.; Yip, H.-L.; Chen, H.; Li, C.-Z. High-Performance See-through Power Windows. *Energy Environ. Sci.* **2022**, *15* (6), 2629–2637.

(35) Liang, N.; Tian, R.; Xu, Y.; Yao, H.; Yang, H.; Wei, Y.; Xin, X.; Chen, R.; Zhai, T.; Wang, Z.; Hou, J. Trans-Reflective Structural Color Filters Assisting Multifunctional-Integrated Semitransparent Photovoltaic Window. *Adv. Mater.* **2023**, *35* (22), 2300360.

(36) Zhang, J.; Xu, G.; Tao, F.; Zeng, G.; Zhang, M.; Yang, Y. M.; Li, Y.; Li, Y. Highly Efficient Semitransparent Organic Solar Cells with Color Rendering Index Approaching 100. *Adv. Mater.* **2019**, *31* (10), 1807159.

(37) Xu, X.; Wei, Q.; Zhou, Z.; He, H.; Tian, J.; Yip, H.; Fu, Y.; Lu, X.; Zhou, Y.; Li, Y.; Zou, Y. Efficient Semitransparent Organic Solar Cells with CRI over 90% Enabled by an Ultralow-Bandgap A-DA'D-A Small Molecule Acceptor. *Adv Funct Materials* **2023**, 2305017.

(38) Yang, H.; Liang, N.; Wang, J.; Chen, R.; Tian, R.; Xin, X.; Zhai, T.; Hou, J. Transfer-Printing a Surface-Truncated Photonic Crystal for Multifunction-Integrated Photovoltaic Window. *Nano Energy* **2023**, *112*, 108472.

(39) Xia, R.; Brabec, C. J.; Yip, H.-L.; Cao, Y. High-Throughput Optical Screening for Efficient Semitransparent Organic Solar Cells. *Joule* **2019**, *3* (9), 2241–2254.

(40) Xu, T.; Deng, B.; Zhao, Y.; Wang, Z.; Lévêque, G.; Lambert, Y.; Grandidier, B.; Wang, S.; Zhu, F. High-Throughput Computing Guided Low/High Index Optical Coupling Layer for Record-Performance Semitransparent Organic Solar Cells. *Adv. Energy Mater.* **2023**, *13* (35), 2301367.

(41) Deng, B.; Lian, H.; Xue, B.; Song, R.; Chen, S.; Wang, Z.; Xu, T.; Dong, H.; Wang, S. Niobium-Carbide MXene Modified Hybrid Hole Transport Layer Enabling High-Performance Organic Solar Cells Over 19%. *Small* **2023**, *19* (23), 2207505.

(42) Lian, H.; Pan, M.; Han, J.; Cheng, X.; Liang, J.; Hua, W.; Qu, Y.; Wu, Y.; Dong, Q.; Wei, B.; Yan, H.; Wong, W.-Y. A $MoSe_2$ Quantum Dot Modified Hole Extraction Layer Enables Binary Organic Solar Cells with Improved Efficiency and Stability. *J. Mater. Chem. A* **2021**, *9* (30), 16500–16509.

(43) Wang, J.; Wang, Y.; Bi, P.; Chen, Z.; Qiao, J.; Li, J.; Wang, W.; Zheng, Z.; Zhang, S.; Hao, X.; Hou, J. Binary Organic Solar Cells with 19.2% Efficiency Enabled by Solid Additive. *Adv. Mater.* **2023**, *35* (25), 2301583.

(44) Chen, L.; Yi, J.; Ma, R.; Ding, L.; Dela Peña, T. A.; Liu, H.; Chen, J.; Zhang, C.; Zhao, C.; Lu, W.; Wei, Q.; Zhao, B.; Hu, H.; Wu, J.; Ma, Z.; Lu, X.; Li, M.; Zhang, G.; Li, G.; Yan, H. An Isomeric Solid Additive Enables High-Efficiency Polymer Solar Cells Developed Using a Benzo-Difuran-Based Donor Polymer. *Adv. Mater.* **2023**, *35* (26), 2301231.

(45) Stolz, S.; Petzoldt, M.; Kotadiya, N.; Rödlmeier, T.; Eckstein, R.; Freudenberg, J.; Bunz, U. H. F.; Lemmer, U.; Mankel, E.; Hamburger, M.; Hernandez-Sosa, G. One-Step Additive Crosslinking of Conjugated Polyelectrolyte Interlayers: Improved Lifetime and Performance of Solution-Processed OLEDs. *J. Mater. Chem. C* **2016**, *4*, 11150–11156.

(46) Song, J.; Zhu, L.; Li, C.; Xu, J.; Wu, H.; Zhang, X.; Zhang, Y.; Tang, Z.; Liu, F.; Sun, Y. High-Efficiency Organic Solar Cells with Low Voltage Loss Induced by Solvent Additive Strategy. *Matter* **2021**, *4* (7), 2542–2552.

(47) Huang, Y.; Xing, J.; Gong, Q.; Chen, L.-C.; Liu, G.; Yao, C.; Wang, Z.; Zhang, H.-L.; Chen, Z.; Zhang, Q. Reducing Aggregation Caused Quenching Effect through Co-Assembly of PAH Chromophores and Molecular Barriers. *Nat. Commun.* **2019**, *10* (1), 169.

(48) Fu, J.; Fong, P. W. K.; Liu, H.; Huang, C.-S.; Lu, X.; Lu, S.; Abdelsamie, M.; Kodalle, T.; Sutter-Fella, C. M.; Yang, Y.; Li, G. 19.31% Binary Organic Solar Cell and Low Non-Radiative Recombination Enabled by Non-Monotonic Intermediate State Transition. *Nat. Commun.* **2023**, *14* (1), 1760.

(49) Hu, Z.; Wang, J.; Wang, Z.; Gao, W.; An, Q.; Zhang, M.; Ma, X.; Wang, J.; Miao, J.;

Yang, C.; Zhang, F. Semitransparent Ternary Nonfullerene Polymer Solar Cells Exhibiting 9.40% Efficiency and 24.6% Average Visible Transmittance. *Nano Energy* **2019**, *55*, 424–432.

(50) Xu, T.; Luo, Y.; Wu, S.; Deng, B.; Chen, S.; Zhong, Y.; Wang, S.; Lévêque, G.; Bachelot, R.; Zhu, F. High-Performance Semitransparent Organic Solar Cells: From Competing Indexes of Transparency and Efficiency Perspectives. *Adv. Sci.* **2022**, *9* (26), 2202150.

(51) Peng, Y.; Lai, J.-C.; Xiao, X.; Jin, W.; Zhou, J.; Yang, Y.; Gao, X.; Tang, J.; Fan, L.; Fan, S.; Bao, Z.; Cui, Y. Colorful Low-Emissivity Paints for Space Heating and Cooling Energy Savings. *Proc. Natl. Acad. Sci. U.S.A.* **2023**, *120* (34), e2300856120.